Wake Dynamics and Rotor–Fuselage Aerodynamic Interactions

Adam R. Kenyon
Postgraduate Research Student
Imperial College, London, UK

Richard E. Brown*
Mechan Chair of Engineering
University of Glasgow, Glasgow, UK

The unsteady loads experienced by a helicopter are known to be strongly influenced by aerodynamic interactions between the rotor and fuselage; these unsteady loads can lead to deficiencies in handling qualities and unacceptable vibratory characteristics of the rotorcraft. This work uses a vorticity-based computational model to study the governing processes that underpin this aerodynamic interaction and aims to provide greater understanding of the wake dynamics in the presence of a fuselage, as well as an appreciation of how the geometry of the wake affects the loading on the fuselage. The well-known experiments using NASA's ROBIN fuselage are used to assess the accuracy of the computations. Comparisons of calculations against results from smoke visualization experiments are used to demonstrate the ability of the model to reproduce accurately the geometry of the rotor wake, and comparisons with inflow data from the experiments show the method to capture well the velocity field near to the rotor. The fuselage model is able to predict accurately the unsteady fuselage loading that is induced by blade passage and also by the inviscid interaction between the main rotor wake and fuselage.

Nomenclature

A	matrix of influence coefficients
A_0	collective pitch, deg
A_1	lateral cyclic pitch, deg
B_1	longitudinal cyclic pitch, deg
c	blade chord, inches
C_P	pressure coefficient $\frac{p - p_\infty}{\frac{1}{2}\rho U_\infty^2}$
$C_P{}'$	modified pressure coefficient $100 \times \frac{p - p_\infty}{\frac{1}{2}\rho(\Omega R)^2}$
e	flap hinge offset, inches
I_β	blade flapping inertia, slug ft^2
l	fuselage half-length, inches
M_B	blade mass, lb
N	number of fuselage panels
N_B	number of blades
R	rotor radius, inches
r_c	blade root cutout, inches
TPP	tip path plane
$\mathbf{U}_\infty$	freestream velocity, ft/s
$\mathbf{u}$	local velocity ft/s
V_{tip}	rotor tip speed ft/s
$\mathbf{w}$	wake-induced velocity ft/s
α_s	shaft tilt (positive aft), deg
β_0	coning angle, deg
Γ	matrix of vortex loop strengths
λ_i	induced inflow normal to TPP (positive downward)
μ	advance ratio
μ_i	induced inflow parallel to TPP (positive aft)
σ	rotor solidity
ψ	blade azimuth angle, deg
Ω	main rotor speed, rpm

*Corresponding author; email: r.brown@aero.gla.ac.uk.
Manuscript received April 2007; accepted August 2008.

Introduction

The aerodynamic interactions between the rotor and the fuselage of a helicopter can have a significant influence on both the steady and the vibratory loads experienced by both components of the system. This interaction can thus affect the performance, dynamics, and handling qualities of the helicopter. The direct impingement of the rotor wake on the fuselage has a particularly strong effect on the characteristics of the system (Ref. 1). The development of the Boeing YUH-61 UTTAS helicopter in the 1960s provides an example of the extent to which the aerodynamic interactions between the rotor and fuselage can influence the design of the helicopter. The original YUH-61 design featured very low fuselage–rotor separation, which caused unexpectedly high blade loads and fuselage vibration during initial flight tests. Wind tunnel experiments were used to identify the causes of the vibration and to evaluate various solutions to the problem, but the aircraft was never accepted into service. A major goal of current computational research is to provide predictive techniques that are capable of identifying and mitigating potential interactional problems before they are encountered during flight test, and thus to avoid some of the expensive mistakes of the past.

Many attempts have been made to develop models that are capable of capturing accurately the aerodynamic interactions between the rotor and fuselage of both generic and actual helicopter configurations, and a variety of approaches have been adopted. The simplest approach has been to use a prescribed or free wake technique coupled to a potential flow representation of the fuselage (e.g., Refs. 2–5). These methods have yielded

DOI: 10.4050/JAHS.54.012003

valuable physical insight into the problem and have the advantage of being computationally inexpensive, but are limited in their ability to capture accurately the wake geometry (particularly as the wake nears the fuselage) and do not naturally model viscous flow features on the fuselage.

Current limitations in computational resources demand that major simplifying assumptions be made to enable full rotorcraft simulations to be tractable. Recently, work has been conducted on modeling the fuselage with Euler/Navier–Stokes methods and using a simplified representation of the rotor (e.g., using actuator disks) in an attempt to accurately predict fuselage forces (e.g., Refs. 6, 7). This approach is able to model viscous phenomena on the fuselage, but because of the simplification of the rotor system, it is limited in its ability to capture the geometry of the rotor wake and therefore the detailed influence of the rotor wake on the fuselage loading. For the same reasons, the approach is also unable to capture the precise influence of the fuselage on the rotor. The simplifications required to simulate full rotorcraft configurations have been reduced by the development of various CFD techniques such as overset grids and sliding meshes, which permit relative motion between the rotor and fuselage (e.g., Refs. 8–10) and thus pave the way toward concurrent high-resolution CFD modeling of both the rotor and the fuselage. When solving the Euler/Navier–Stokes equations in primitive variable form, however, the number of computational cells required to maintain vortical flow features for the many rotor revolutions required to capture accurately the interaction between the rotor wake and fuselage still needs to be very large if numerical dissipation of the vorticity field is to be avoided.

Methods based on the solution of the Navier–Stokes equations in vorticity–velocity form, such as Brown's vorticity transport model, are capable of preserving the vortical structures in the rotor wake for many rotor revolutions and are thus well suited to the modeling of rotor–fuselage interactions. The use of hybrid methods is a new and potentially powerful technique whereby a primitive variable Navier–Stokes method for modeling the flow near aerodynamic surfaces such as the fuselage and rotor blades is coupled to a vorticity-based wake model in an attempt to exploit the advantages of both approaches (e.g., Ref. 11). This paper will show, through comparison with the experimental data, that the rotor wake trajectory and wake-induced inflow can both be captured accurately using the vorticity transport approach. Both the steady and the unsteady components of the loading on the fuselage are well represented using this computational approach. The strong influence of individual wake vortices on the amplitude and form of the unsteady pressure distribution on the fuselage, particularly when these vortices come into close proximity to the fuselage, shows clearly the importance of modeling correctly the dynamics of the wake when simulating the aerodynamic interaction between the rotor and the fuselage of any helicopter.

Modeling

The aerodynamic environment surrounding NASA's ROBIN model rotor–body system (Ref. 12) has been simulated using the vorticity transport model (VTM), developed by Brown (Ref. 13) and extended by Brown and Line (Ref. 14). A full description of the model is contained within the original references; for the sake of brevity only the basic characteristics of the model are summarized here.

The VTM evolves the vorticity–velocity form

$$\frac{\partial}{\partial t}\omega + \mathbf{u}\cdot\nabla\omega - \omega\cdot\nabla\mathbf{u} = S + \nu\nabla^2\omega \tag{1}$$

of the Navier–Stokes equations on a Cartesian grid surrounding the rotorcraft. Significant savings in memory and computational time are achieved by allowing the distribution of cells within the computational domain to track the vorticity field as it evolves. This is done by creating computational cells in regions of the flow, where vorticity exists and subsequently destroying them once the vorticity migrates elsewhere. Computational efficiency is enhanced further by using a sequence of nested grids in which the cells within the outer grids are arranged to be coarser than those closer to the rotor. This reduces the overall cell count while allowing a highly resolved flow field to be maintained near the rotor. The convection algorithm implemented in the VTM is particularly effective in controlling the local rate of dissipation of the vorticity, allowing the integrity of vortical structures in the rotor wake to be preserved for many rotor revolutions. The VTM is thus particularly well suited to resolving the wake-induced interactions between geometrically well-separated components of the helicopter. In the context of the present paper, this property of the model enables the long-range aerodynamic interactions between the rotor and fuselage of the ROBIN configuration to be studied in detail.

In the version of the VTM used to generate the results presented in this paper, the blade aerodynamics are modeled using an extension of the Weissinger-L version of lifting line theory. In this approach, the two-dimensional aerodynamic characteristics of the rotor blade sections are specified in a lookup table as a function of angle of attack and Mach number for a given Reynolds number. These characteristics are then enforced by applying a modified zero through-flow condition at a set of aerodynamic stations along the length of each blade. Even though blade stall can be modeled using this technique, the approach is still essentially inviscid. The profile drag of the blade is thus calculated as a separate function of local angle of attack and then added to the local aerodynamic force that is calculated from the lifting line model.

Given the relatively high Reynolds number of the systems of interest in this study, the viscous diffusion is assumed to be negligible within the wake and hence the fluid viscosity ν is set equal to zero. The vorticity source S is then solely due to the lifting surfaces immersed within the flow; in the current implementation, the fuselage is not considered a lifting surface and thus contributes zero net vorticity to the flow. The source can thus be written in terms of the temporal and spatial variation of bound vorticity, ω_b, on the blades as

$$S = -\frac{d}{\mathrm{d}\,t}\omega_\mathrm{b} + \mathbf{u}_\mathrm{b}\nabla\cdot\omega_\mathrm{b} \tag{2}$$

The velocity field is related to the vorticity field using a fast multipole method to invert the differential form of the Biot–Savart law,

$$\nabla^2\mathbf{u} = -\nabla\times\omega \tag{3}$$

A Lagrangian formulation is used to model the motion of the blades within the VTM, allowing fully articulated rotor hubs and flexible blades to be modeled if necessary.

To model the presence of a fuselage, the fuselage surface is discretized into a system of N quadrilateral panels. Each panel edge is represented as a vortex filament of constant strength Γ_i, with the filaments on each panel i thus forming a closed loop of vorticity. The velocity at any panel centroid is then given by the sum of the influences from all vortex filaments on the body together with the freestream component of velocity, $\mathbf{U}_\infty$, and the velocity $\mathbf{w}$ that is induced by any other vorticity within the flow. A boundary condition of zero through flow is enforced simultaneously at the centroids of all panels, so that

$$(\mathbf{U}_\infty + \mathbf{w})_i\cdot\mathbf{n}_i + \sum_{j=1}^{N} A_{ij}\Gamma_j = 0 \tag{4}$$

where $\mathbf{n}_i$ is the unit vector normal to panel i. This linear equation is solved at each computational timestep to obtain the matrix of vortex loop strengths, Γ. The influence matrix, A, accounts for the velocity induced on each panel by every other panel and is thus of size $N\times N$.

The fact that the fuselage is a closed surface provides an additional, but implicit, constraint on the relationship between the panel strengths, by requiring that they should sum to zero, that results in A being singular. In the VTM, the vortex loop strengths are thus evaluated using an approximation to the inverse of A that is obtained using singular value decomposition. A considerable saving in computational effort is achieved by assuming the fuselage to be rigid. This is because the matrix of influence coefficients then does not change with time, allowing the inversion of A to be performed prior to the simulation.

The pressure on the fuselage surface is calculated from the unsteady Bernoulli equation,

$$\frac{p - p_\infty}{\frac{1}{2}\rho} = |\mathbf{U}_\infty|^2 - |\mathbf{u}|^2 - 2\frac{\partial \phi}{\partial t} \tag{5}$$

In the VTM, the change in panel strengths with time as well as the disturbance to the velocity potential due to the convection of vortices within the wake is accounted for when evaluating the unsteady potential term $\partial\phi/\partial t$. Similarly, the contribution from all the vorticity in the computational domain, as well as a near-field correction term that accounts for the self-influence of the vorticity on each panel by assuming it to be distributed as an equivalent vortex sheet, is accounted for when evaluating the velocity $\mathbf{u}$ on the surface of the fuselage.

All simulations presented in this paper were, unless otherwise stated, performed with 30 aerodynamic stations along the length of each blade and 50 grid cells per rotor radius; where present, the fuselage was modeled using a total of 2174 body panels. These values were chosen as a compromise between simulation CPU time and the ability of the model to resolve small-scale flow features of interest. The dependency of the calculation on grid resolution has been checked, with results for the predicted inflow through the rotor shown to change very little if the resolution is increased much beyond this.

ROBIN Fuselage Experiments

The ROtor Body INteraction (ROBIN) fuselage, developed by NASA, has been used in many previous experimental and numerical studies into rotor–fuselage interactions (e.g., Refs. 7,8,12,15). The ROBIN body is an analytically defined surface, described by a set of superellipse equations, that is representative of a helicopter fuselage but is also simple enough to be amenable to computational studies. The analytic definition of the fuselage is given in Ref. 12. Essentially, the fuselage consists of a slender, streamlined main body; a small, relatively blunt fairing, traditionally referred to in the ROBIN literature as the "doghouse," is mounted on its upper surface. Experimental data that is available in the literature includes laser-Doppler velocimetry (LDV) of the inflow through the rotor disk (Refs. 15–17), smoke visualizations of the rotor wake (Ref. 18), and steady and time-resolved measurements of fuselage surface pressures (Refs. 12,19).

Three experimental setups were adopted at various times for the various published ROBIN studies. The 2-m rotor test system (2MRTS) was mounted internally to the fuselage; this setup was used for all investigations into vortex trajectories and rotor inflow, and is described in detail in Ref. 20. The externally mounted isolated rotor test system (IRTS) was used to investigate the pressures on the surface of the ROBIN fuselage (Ref. 12). The two systems vary subtly in geometry, as described in Table 1, and the variations need to be taken into account when simulating the experiments. The general rotor model system (GRMS) configuration was used during experiments to obtain measurements of the steady pressures on the isolated ROBIN fuselage (Ref. 19). In the present simulations, however, no attempt was made to model the actual hub geometry or the attachment of the model to the wind tunnel.

Table 1. Simulated helicopter geometry

		Hub Coordinates		
Experiment	Fuselage Yaw	x/l	y/l	z/l
IRTS	1.2°	0.697	0.051	0.322
2MRTS	0.0°	0.697	0.000	0.275
GRMS	Not modeled			

Table 2. Rotor–fuselage parameters used in VTM simulations

Blade section	NACA0012
c (inches)	2.7
Rotor rotation	CCW from above
e/R	0.06
Fuselage shape	ROBIN
I_β (slug/ft^2)	0.046
I (inches)	39.35
Linear twist	−8°
M_B (lb)	0.572
N_B	4
Planform	rectangular
R (inches)	33.88
r_c/R	0.24
σ	0.098

The rotor blades used in the ROBIN experiments were chosen to be very stiff so as to reduce any aerodynamic uncertainty that might be induced by blade flexure (Ref. 21). The blades were thus modeled in the simulations as being rigid. The dynamics of the articulated rotor hub of the IRTS and 2MRTS was fully accounted for, however. Various blade geometries were tested in conjunction with the ROBIN fuselage; in the present study only the rectangular blades with the characteristics detailed in Table 2 were simulated. In all simulations, the rotor was trimmed to the experimentally measured thrust coefficient. The rotor was also trimmed to zero flapping with respect to the shaft, as was the case in the experiments. The fuselage was yawed 1.2° nose left, as described in Ref. 12, when simulating the experiments with the IRTS system. For simulations with the 2MRTS system, the fuselage was not yawed.

Flow features

The distortion of the rotor wake due to the presence of the fuselage significantly affects the inflow through the rotor. The rotor wake also causes unsteady fluctuations in the velocity field around the fuselage that yields an unsteady component to its loading. The accuracy of any simulation technique is therefore highly dependent on its ability to capture the geometry of the rotor wake as it passes around the fuselage.

The geometries of the VTM-simulated wakes of the ROBIN system at various forward flight speeds are shown in Fig. 1. Simulations were performed solely with the IRTS rotor system at an advance ratio $\mu = 0.05$, and solely with the 2MRTS system at $\mu = 0.30$. Although simulations were performed with both the 2MRTS and IRTS rotor configurations at $\mu = 0.15$ and 0.23, only the simulations of the 2MRTS system are shown here to demonstrate the more pronounced interactions between the wake and fuselage due to the reduced separation between rotor hub and fuselage for this configuration.

The simulated wake at $\mu = 0.05$ distorts significantly as it engulfs large parts of the fuselage. Interestingly, a well-ordered and steady wake could not be established in the simulations at this flight condition, even after running for a significant number of rotor revolutions. At advance

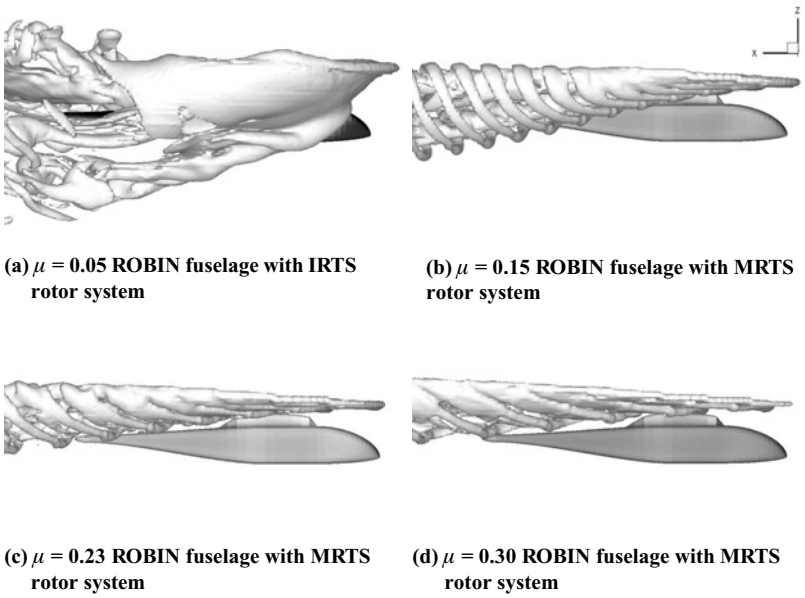

(a) μ = 0.05 ROBIN fuselage with IRTS rotor system

(b) μ = 0.15 ROBIN fuselage with MRTS rotor system

(c) μ = 0.23 ROBIN fuselage with MRTS rotor system

(d) μ = 0.30 ROBIN fuselage with MRTS rotor system

Fig. 1. Wake structure at various forward flight speeds.

ratios of 0.15 and greater, simulations suggest that the rotor wake in the various experiments was skewed back so far that only the rear of the ROBIN fuselage was in close proximity to it (Figs. 1(b)–1(d)). At advance ratio $\mu = 0.15$, the wake impinges directly on the tail of the fuselage as shown in Fig. 1(b); this direct impingement is not seen in the simulations at higher advance ratios.

Fuselage Pressure Distributions

Freeman and Mineck (Ref. 19) measured steady pressures at various points on the surface of the ROBIN fuselage. In their experiments, the ROBIN body was fixed around the GRMS rotor system mounted in the Langley 14 × 22-foot subsonic tunnel, and pressures were recorded at a number of locations along the length of the fuselage both with the rotor blades attached and with the blades removed from the rotor hub. These data have been used to assess the ability of the essentially inviscid fuselage model currently used within the VTM to predict the steady pressure distribution over the isolated ROBIN fuselage. Figure 2 shows the variation of pressure coefficient with vertical height at several axial stations along the length of the fuselage (refer to Fig. 3 to locate these stations with respect to the various geometric features of the ROBIN fuselage) with the fuselage at zero angle of attack and with zero yaw. Generally, the predicted variation of pressure coefficient agrees very closely with the experimental data. The rather subtle deterioration in correlation at certain locations toward the tail of the fuselage is attributed to the assumption of inviscid flow in the simulations. Neither the rotor hub nor the strut used in the wind tunnel to support the fuselage was modeled in this simulation. The absence of the strut is believed to account for some of the discrepancy, particularly on the lower part of the fuselage. It is expected that the bluff strut would provide a blockage to the flow and would shed a wake; the effect of these processes in reducing the correlation between experiment and simulation is most pronounced at the station $x/l = 1.16$, but is localized to the two experimental pressure taps closest to the bottom centerline of the fuselage. The omission of the strut from the simulations can thus be reasonably well justified in terms of the minimal effect that this simplification produces on the predicted results. Indeed, the close agreement between the VTM predictions and the measured distribution of pressure over most of the length of the isolated ROBIN fuselage suggests that the inviscid assumption is sufficient to yield a very good representation of the fuselage pressures in all but a few isolated locations.

The presence of the rotor significantly affects the aerodynamic environment in which the fuselage operates. The long-range effect of the bound circulation associated with the rotating blades is to provide a periodic disturbance to the pressures on the fuselage, and the wake produced by the rotor can, under certain flight conditions, pass close enough to the fuselage to create large local disturbances to the pressure distribution on its surface. Mineck and Althoff Gorton (Ref. 12) measured steady and time-resolved pressures on the ROBIN fuselage in the presence of the IRTS rotor system. The experiments were conducted at a number of thrust coefficients and advance ratios; their results are used here to assess the ability of the VTM to predict the unsteady pressures that arise on the fuselage as a result of the interaction with the rotor and its wake. Table 3 lists the flight conditions at which the interaction between the rotor and the fuselage of the ROBIN configuration has been investigated using the VTM.

In rotorcraft applications, a modified pressure coefficient is often used for convenience instead of the standard pressure coefficient. The modified pressure coefficient is nondimensionalized by rotor tip speed rather than the freestream velocity to avoid division by zero at hover and is scaled by a factor of 100 purely for numerical convenience. In all plots of unsteady fuselage pressure presented in this paper, this modified pressure coefficient has been used and the mean value of the pressure has been subtracted from the signal. It should also be noted that all the experimental fuselage pressure data presented in this paper have been shifted in phase by 252° relative to the data published in Ref. 12. This phase lag is generally accepted within the community to have been due to delays in the data acquisition equipment that was used in the experiment (Ref. 22).

All the experimental fuselage pressure data contained in the published literature have been preprocessed by phase averaging over 30 rotor revolutions. A blade-to-blade variability of up to 40% in magnitude is

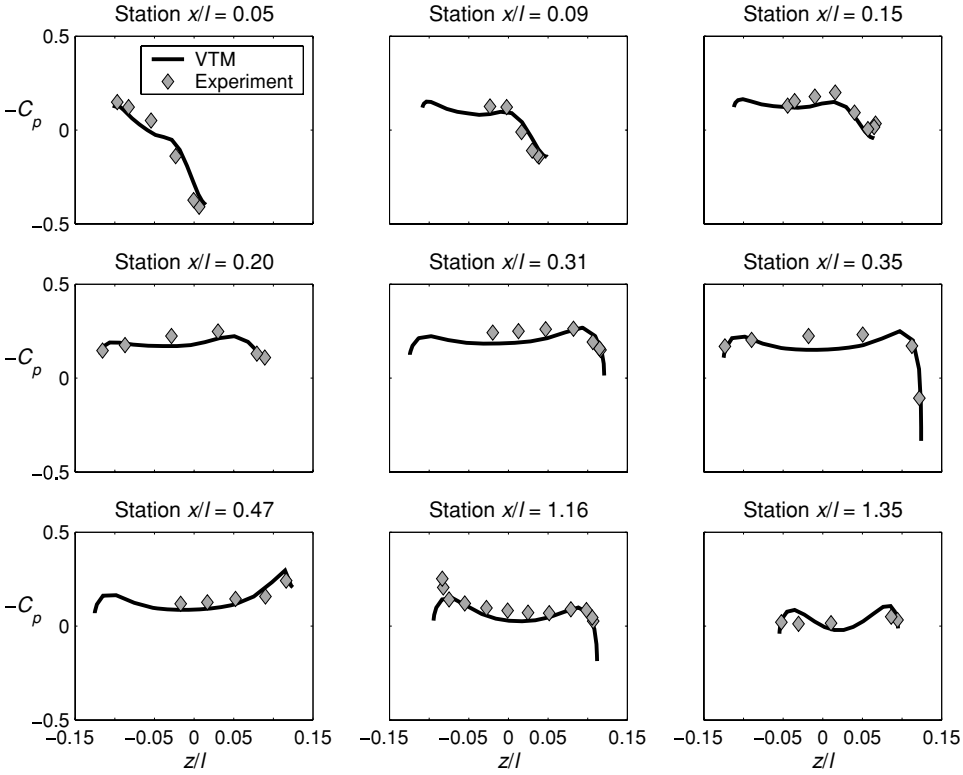

Fig. 2. Pressures on the isolated ROBIN fuselage at various locations along its length.

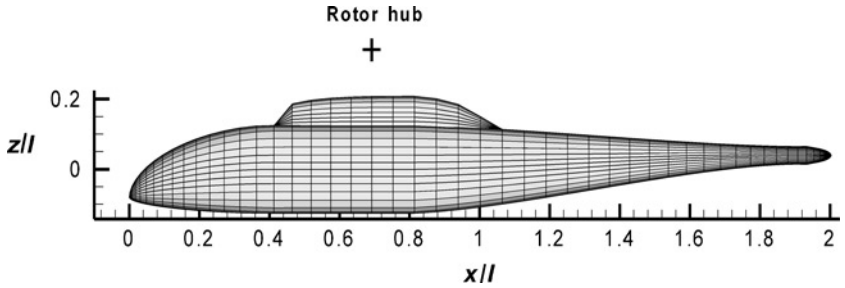

Fig. 3. Coordinate system used to locate the positions of the pressure taps on the ROBIN fuselage.

Table 3. Test cases for pressure experiments (angles in degrees)

	Experiment					Simulation				
μ	C_T	α_s	A_0	A_1	B_1	C_T	α_s	A_0	A_1	B_1
0.05	0.0064	0.0	11.9	−1.3	1.3	0.0064	0.0	6.8	−2.3	1.2
0.15	0.0064	−3.0	10.3	−2.7	2.4	0.0064	−3.0	6.3	−2.3	2.1
0.23	0.0040	−3.0	8.2	−0.5	3.8	0.0040	−3.0	4.3	−1.5	2.1
0.23	0.0064	−3.0	10.4	−0.4	3.8	0.0064	−3.0	6.3	−2.1	3.3
0.23	0.0080	−3.0	11.9	−1.3	4.0	0.0080	−3.0	7.9	−2.6	4.3

known to persist at certain positions on the fuselage, however, despite the averaging process. It should be borne in mind that the VTM data against which this experimental data are compared in this paper are extracted from a single rotor revolution and hence no similar averaging process to that applied to the experimental data has been performed. The simulations were run for typically 40 rotor revolutions. This generally allowed sufficient time for the simulations to reach a reasonably steady state in which the blade-to-blade variation in the output from the simulations could be ignored. As mentioned earlier though, a steady state was never achieved for the simulation at $\mu = 0.05$; similarly, the experimental data for this case show the greatest blade-to-blade variability. Although not pursued further in this paper, this observation does suggest, however, that the predicted unsteadiness in the wake, particularly at very low advance ratio, may be physical in origin, and thus that the averaging procedure used to postprocess the experimental data may be responsible for obscuring some of the relevant physics.

Figures 4–7 illustrate the variation with time of the modified pressure coefficient at various stations along the top centerline of the fuselage (again, refer to Fig. 3 to locate these stations with respect to the various geometric features of the ROBIN fuselage). The VTM-predicted

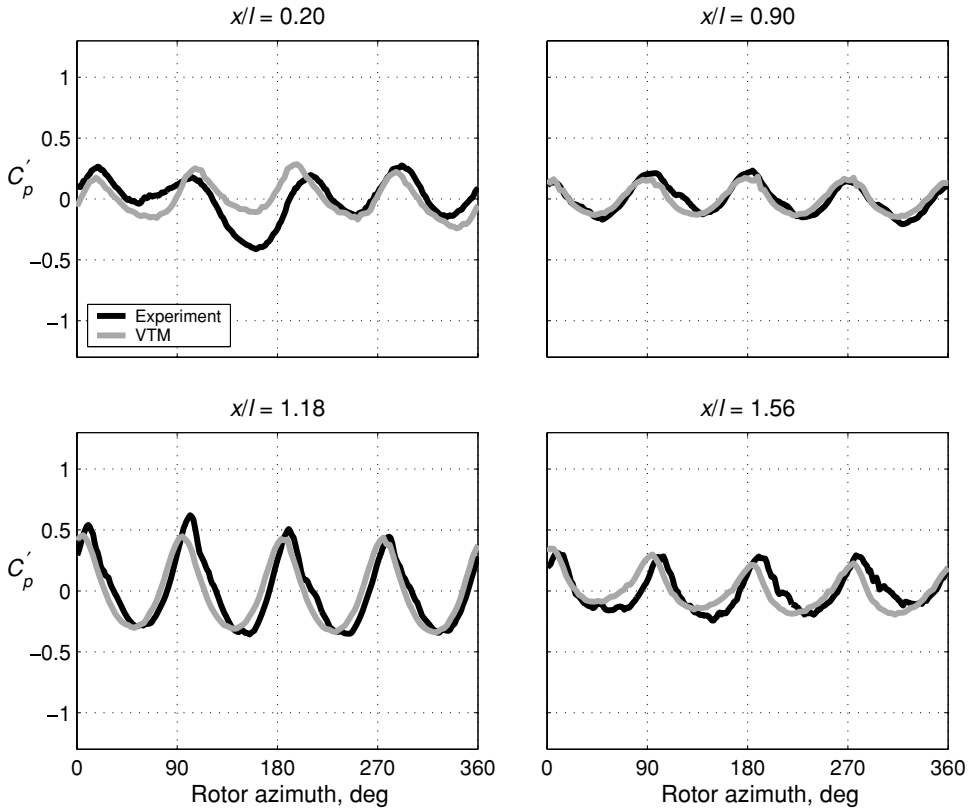

Fig. 4. Variation of pressure with time (rotor azimuth) at various points along the top centerline of the fuselage ($\mu = 0.05$, $C_T = 0.0064$).

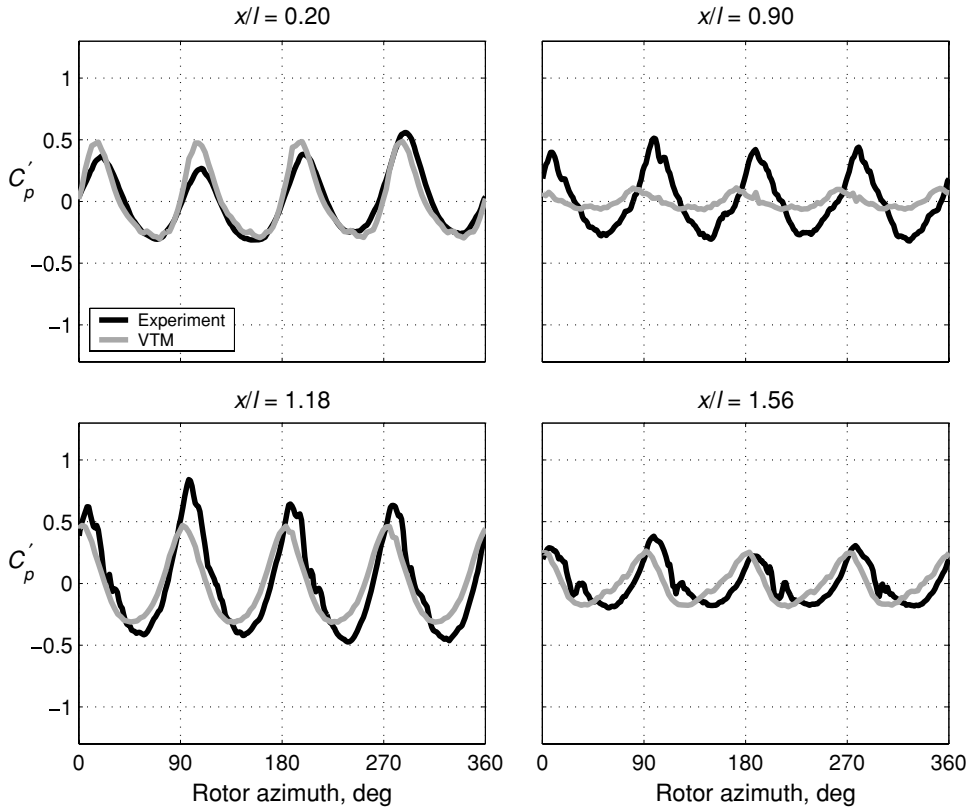

Fig. 5. Variation of pressure with time (rotor azimuth) at various points along the top centerline of the fuselage ($\mu = 0.15$, $C_T = 0.0064$).

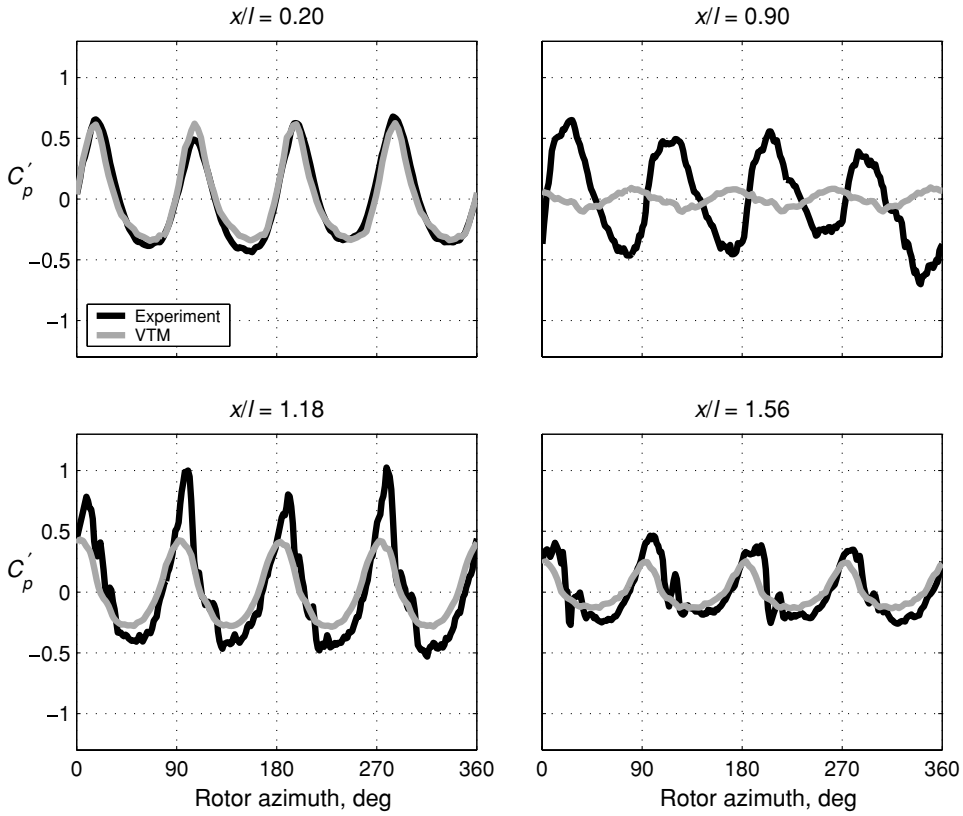

Fig. 6. Variation of pressure with time (rotor azimuth) at various points along the top centerline of the fuselage ($\mu = 0.23$, $C_T = 0.0064$).

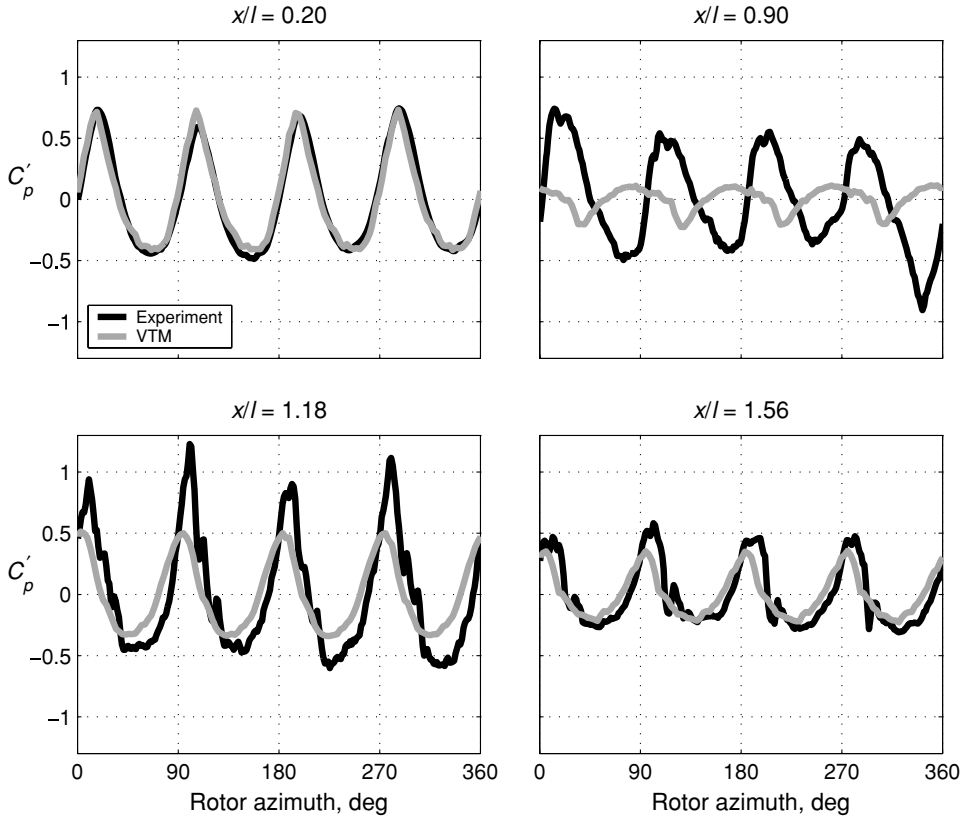

Fig. 7. Variation of pressure with time (rotor azimuth) at various points along the top centerline of the fuselage ($\mu = 0.23$, $C_T = 0.0080$).

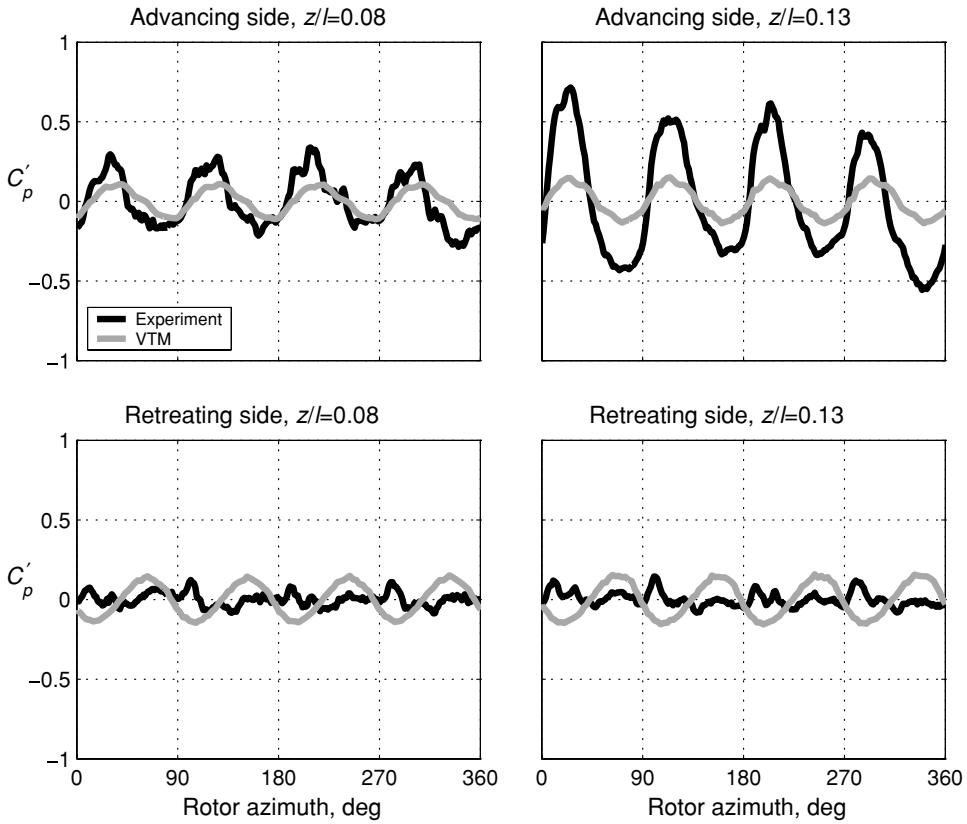

Fig. 8. Variation of pressure with time (rotor azimuth) at various points located around the fuselage at lengthwise station $x/l = 0.90$ ($\mu = 0.15$, $C_T = 0.0064$).

variation of fuselage pressure demonstrates generally very close correlation with the experiment, in terms of both magnitude and phase (after correcting for the known phase lag in the experiments) over the majority of the fuselage and at all the flight conditions listed in Table 3.

The rather pronounced discrepancy in magnitude and phase between the simulated and experimental pressure signal along the top centerline of the fuselage near to the rotor hub (particularly at $x/l = 0.90$ in Figs. 4–7) that arises at advance ratios greater than 0.05 is believed to be due primarily to the absence of any model of the rotor hub in the current simulations. Without a model of the hub, its contributions to the unsteady pressure, particularly those that result from the displacement of the flow around the blade-root attachments, are missing from the simulations.

To help understand more clearly the effect on the simulations of the absence of any model for the rotor hub and blade–root attachments, Fig. 8 shows a comparison between the predicted and measured pressure signals at various points around a loop on the fuselage at an axial location of $x/l = 0.90$, in other words just slightly aft of the rotor hub, with the system operating at a representative advance ratio $\mu = 0.15$. Of particular interest is the strong lateral asymmetry in the amplitude of the measured pressure fluctuations that are induced on the fuselage below the retreating and advancing sides of the rotor disk. This asymmetry is consistent with the larger local pressure disturbance that might be expected to be caused by the blade root attachments as they move against the flow on the advancing side of the rotor rather than, as on the retreating side of the rotor, with the flow. It is indicative that the predicted pressure signatures show very little of the lateral asymmetry that might be expected at this rather sensitive location near the rear of the doghouse were a model of the rotor hub to be included within the simulations.

The current potential flow representation of the fuselage, and particularly the assumption of inviscid flow, is also believed to be partially responsible for the underprediction, in magnitude and in frequency content, of the unsteady pressure immediately behind the doghouse. In particular, several computational analyses of the viscous flow around the ROBIN fuselage (e.g., Ref. 23) predict a small pocket of separated flow just downstream of the relatively bluff doghouse. The presence of such a flow feature would have a significant effect on the pressures measured in this region of the fuselage. Vortex shedding from the doghouse and rotor hub and secondary interactions of the wake with the fuselage boundary layer are believed to be partly responsible for the high-frequency content in the experimental pressure signals toward the rear of the fuselage (e.g., at $x/l = 1.18$); these are both features of the flow that the current version of the VTM is unable to predict.

The presence of frequency content in the pressure signals at greater than the blade-passage harmonic is also characteristic of the passage of individual rotor wake vortices close to the fuselage. Simulations show the strong vortical structures created by the main rotor to pass very close to the fuselage under certain flight conditions, and these vortices to induce large velocity perturbations to the flow near the fuselage. At fixed measurement locations, these disturbances are responsible for the increased frequency content in the pressure signal as seen, for instance, in the lower two plots in Fig. 5. It is known that, under a wide range of circumstances, these perturbations are capable of causing boundary layer separation and the generation of secondary vortices near to the surface (Ref. 24). Prediction of these essentially viscous phenomena is also beyond the capabilities of the current model.

The current model is capable, however, of capturing some of the inviscid effects that result from close interactions between the wake and

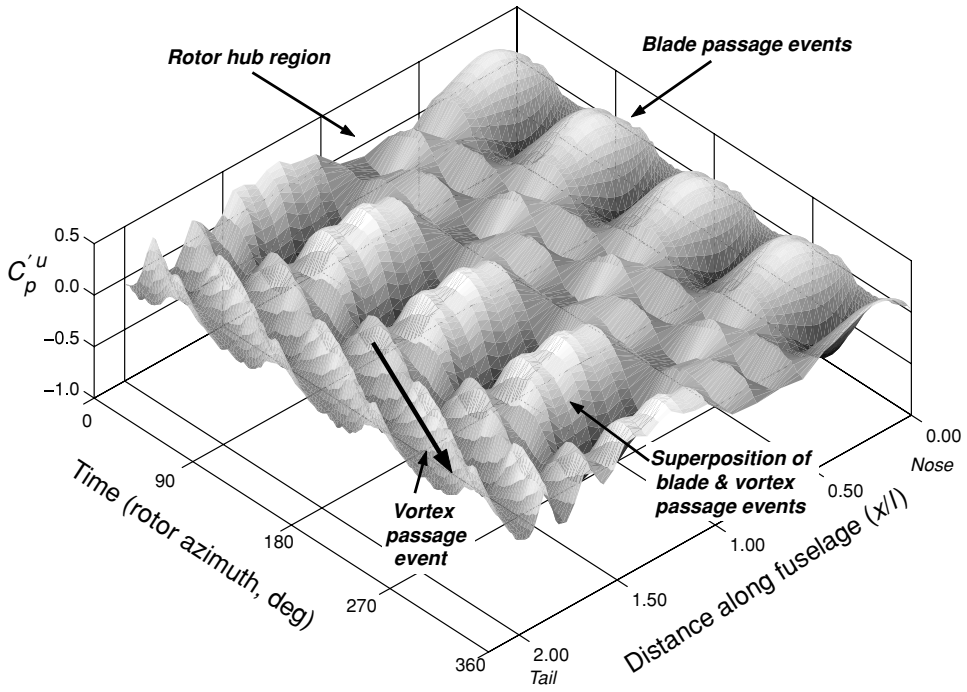

Fig. 9. Visualization of unsteady loading on fuselage top centerline ($\mu = 0.15$, $C_T = 0.0064$).

the fuselage. The effect on the fuselage pressure of the close passage of individual wake vortices just above its surface is visible very clearly in Figs. 9 and 10. In these figures, the VTM-predicted unsteady component, $\partial\phi/\partial t$, of the pressure along the top centerline of the fuselage is plotted as a function of rotor azimuth with the system at advance ratio $\mu = 0.15$. The effect of periodic blade passage is seen along the length of the fuselage as a series of N/rev stationary waves in the pressure signal. These appear in Fig. 10 as a series of approximately horizontal contours. The lateral offset of the rotor from the fuselage in these simulations, which modeled the experimental IRTS configuration, results in the minor phase shift in the peak of the blade passage induced signal between the front and rear of the fuselage. The presence of the root cutout of the rotor is visible as the region of smaller pressure fluctuations that are out of phase with the blade passage features, in the region $x/l = 0.50$–0.90. Aft of the rotor center, the unsteady pressure signature that results from blade passage is modified by the close passage of individual wake vortices, especially in the region $x/l = 1.00$–1.50. The streaming of the individual wake vortices over the rear of the fuselage is visible in Fig. 9 as a series of traveling waves in the pressure distribution toward the rear of the fuselage between $x/l = 1.50$ and $x/l = 2.00$. These features are clearly visible in Fig. 10 as a series of oblique contours near the rear of the fuselage. The rotor extends axially along the fuselage top centerline to approximately $x/l = 1.55$; aft of this location, the effects of vortex close passage are somewhat isolated from the fluctuations in fuselage pressure due to blade passage. These two figures demonstrate conclusively the ability of the VTM to capture the inviscid effects of both blade passage and wake impingement on the pressure on the fuselage, even though the amplitude of the pressure perturbations on the fuselage that are induced by wake impingement appears to be somewhat underpredicted at the present spatial resolution of the computations.

Wake Vortex Trajectories

Smoke visualization of the vortices in the wake of the ROBIN system was performed in the NASA Langley 14 × 22-foot subsonic tunnel (Ref. 18), using the 2MRTS rotor system together with the ROBIN fuselage. Smoke was injected upstream of the test section, and a laser light sheet was used to visualize the flow on longitudinal slices through the rotor wake.

The laser was strobed so that instantaneous vortex positions could be identified. The phase of the strobing was varied from 0° to 90° in 11.25° increments to capture the positions of the wake vortices with the rotor at various azimuths.

The vorticity–velocity formulation of the VTM makes the determination and visualization of the position of wake vortices very straightforward. The vorticity distribution on longitudinal slices through the wake was extracted from the simulated flow field and plotted as the contour maps shown in Figs. 11 and 12. No attempt was made to isolate individual vortex structures, such as tip vortices, from the simulation data. Rather, all vortex structures are plotted for completeness. The individual blade–tip vortices, and their eventual rollup to form larger coherent structures downstream of the rotor as identified in Ref. 18, are all visible in the wake data that are obtained from the VTM simulations.

Figures 11 and 12 show a comparison of experimentally measured vortex trajectories with simulation results for advance ratios of 0.15 and 0.23, respectively. The agreement between experimentally measured and simulated tip vortex position at all lateral locations is very close, although the characteristic initial motion of the tip vortices above the plane of the rotor, indicating an upwash on the outboard sections of the advancing side of the disk, seems to be underpredicted by the VTM calculation. This discrepancy is more pronounced the higher the advance ratio.

Table 4 compares experimentally measured thrust coefficients and control angles with simulated results for this series of experiments. All control angles were predicted to within 1.1° of the experimental values, with the collective pitch and longitudinal cyclic pitch being particularly well matched. This observation contrasts somewhat with the rather poorer agreement between the experimentally measured and VTM-predicted control angles that is presented in Table 3 for the ROBIN pressure experiments, that were described earlier in this paper. For this set of experiments, the simulated collective pitch is consistently 4–5°

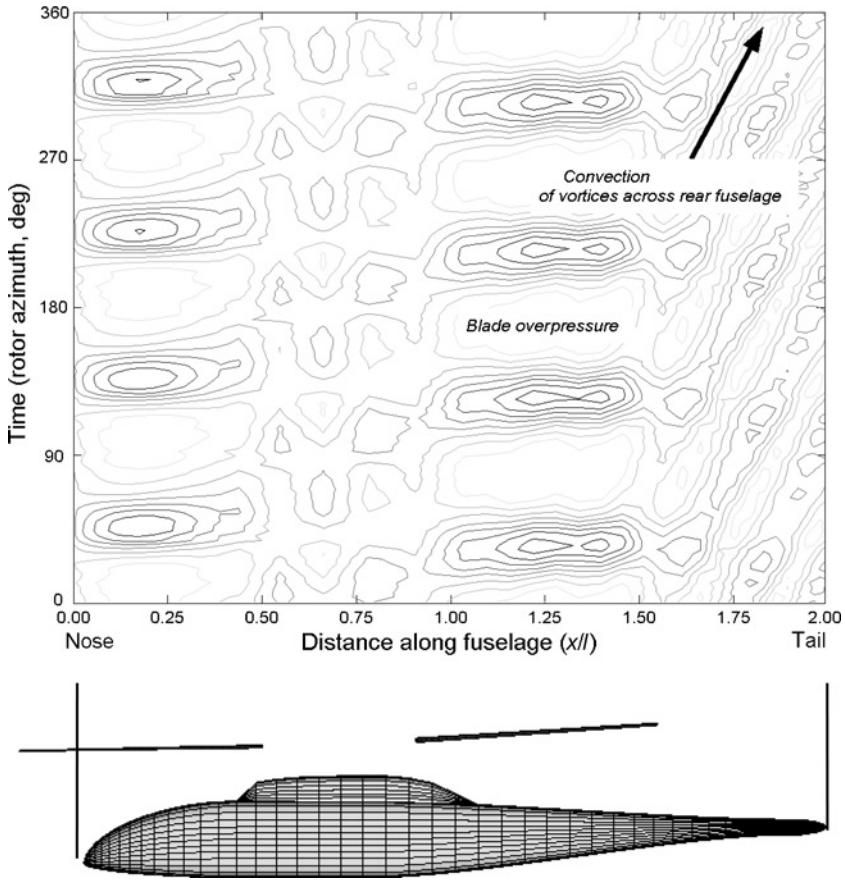

Fig. 10. Contours of unsteady loading on fuselage top centerline ($\mu = 0.15$, $C_T = 0.0064$).

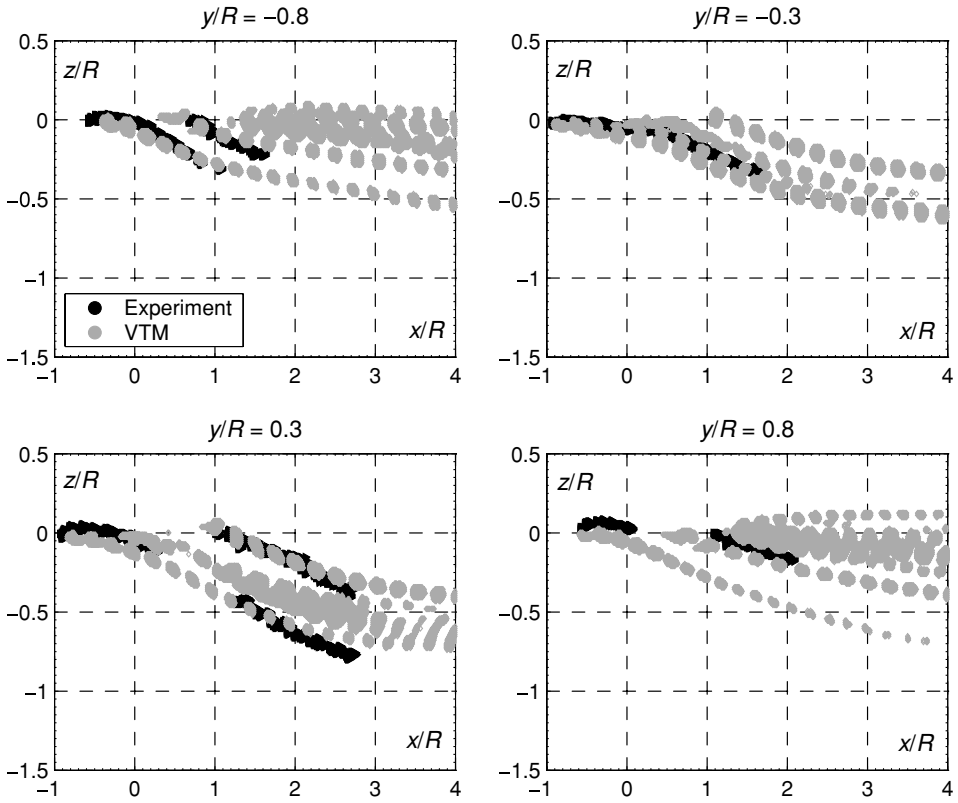

Fig. 11. Vortex trajectories visualized along longitudinal slices through the wake ($\mu = 0.15$, $C_T = 0.0064$).

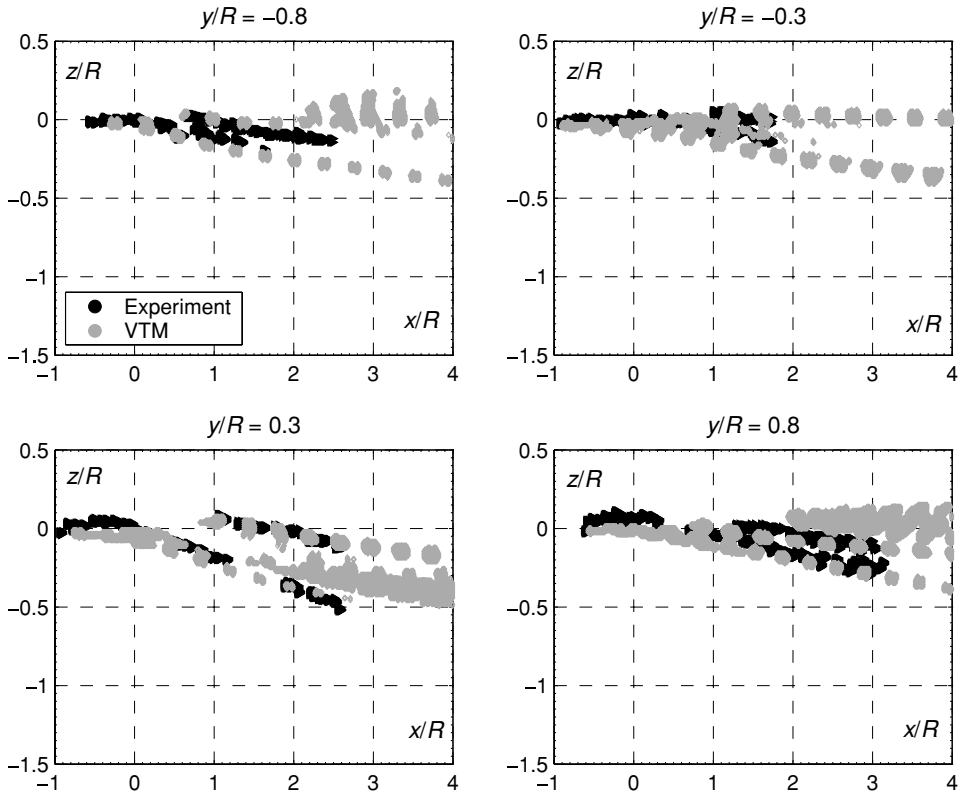

Fig. 12. Vortex trajectories visualized along longitudinal slices through the wake ($\mu = 0.23$, $C_T = 0.0064$).

Table 4. Test cases for smoke visualization experiments (angles in degrees)

	Experiment						Simulation					
μ	C_T	α_s	β_0	A_0	A_1	B_1	C_T	α_s	β_0	A_0	A_1	B_1
0.15	0.0064	−3.0	1.5	6.6	−1.4	2.0	0.0063	−3.0	1.7	6.2	−2.3	2.1
0.23	0.0064	−3.0	1.5	6.5	−1.1	3.2	0.0064	−3.0	1.7	6.3	−2.2	3.4

lower than the experimentally measured values, whereas the lateral cyclic is overpredicted by approximately 2°; the predicted longitudinal cyclic, though, is within 1° of the experimental values in all but one case. It is interesting to note that the variation in experimentally measured control angles between the various tests studied in this paper is of the order of the discrepancies between simulation and experiment. It is difficult, thus, to arrive at any concrete conclusions, using the published ROBIN data, regarding the ability of the VTM to predict the trim state of the rotor system.

Rotor Inflow

Elliott et al. and Althoff et al. (Refs. 15–17,25,26) measured the inflow through a series of rotors with different planform, under various operating conditions, in the presence of the ROBIN fuselage. The comparisons presented here are for their rotor with rectangular planform blades as mounted on the 2MRTS rotor system. In all cases, an LDV system was used to record the induced velocity components normal and parallel to the rotor tip path plane (TPP). Measurements were taken at various azimuthal locations on planes located at various heights (of the order of one blade chord length) above the TPP. The standard deviation of the experimentally measured velocities is available, but is not plotted here so as not to be misinterpreted as an error bound on the experimental data.

A comparison of simulated control angles and thrust coefficients against the data from these experiments is presented in Table 5. The collective pitch is consistently underpredicted by approximately 3°. Both the cyclic control angles are predicted to within 1.2° of the experimental values, however. The discrepancy between experimentally measured control angles between the smoke visualization and inflow experiments is somewhat unexpected though, since both experiments were performed using the 2MRTS configuration and both rotors were trimmed in the same way to the same operating conditions. Taking earlier comments into account, it appears that some doubt should possibly be cast on the consistency of the measurements of the control angles that were obtained during the various ROBIN experiments.

To minimize the effect of any errors in the predicted blade dynamics leading to inaccuracy in the location relative to the rotor of the points at which the inflow was sampled, the numerical data for the inflow generated by the rotor were extracted from the same positions, relative to the TPP of the rotor, at which the experimental data were purported to have been obtained, rather than from a set of absolute coordinates relative to the rotor hub. In any event, the close agreement between the measured and predicted coning angles of the rotor (see Table 5) implies an error in the relative positions of the TPP of the simulated rotor and the experimental system of only about 4% of the blade chord.

Agreement between simulation and experiment for the component of inflow parallel to the rotor, measured on the plane located 1.15c

Table 5. Test cases for inflow experiments (angles in degrees)

	Experiment						Simulation					
μ	C_T	α_s	β_0	A_0	A_1	B_1	C_T	α_s	β_0	A_0	A_1	B_1
0.15	0.0063	−3.0	1.5	9.4	−1.1	3.2	0.0063	−3.0	1.7	6.2	−2.3	2.1
0.23	0.0064	−3.0	1.8	8.2	−1.5	4.1	0.0064	−3.0	1.7	6.3	−2.2	3.4
0.30	0.0065	−4.0	2.1	10.3	−1.6	5.9	0.0065	−4.0	1.7	7.5	−2.2	5.0

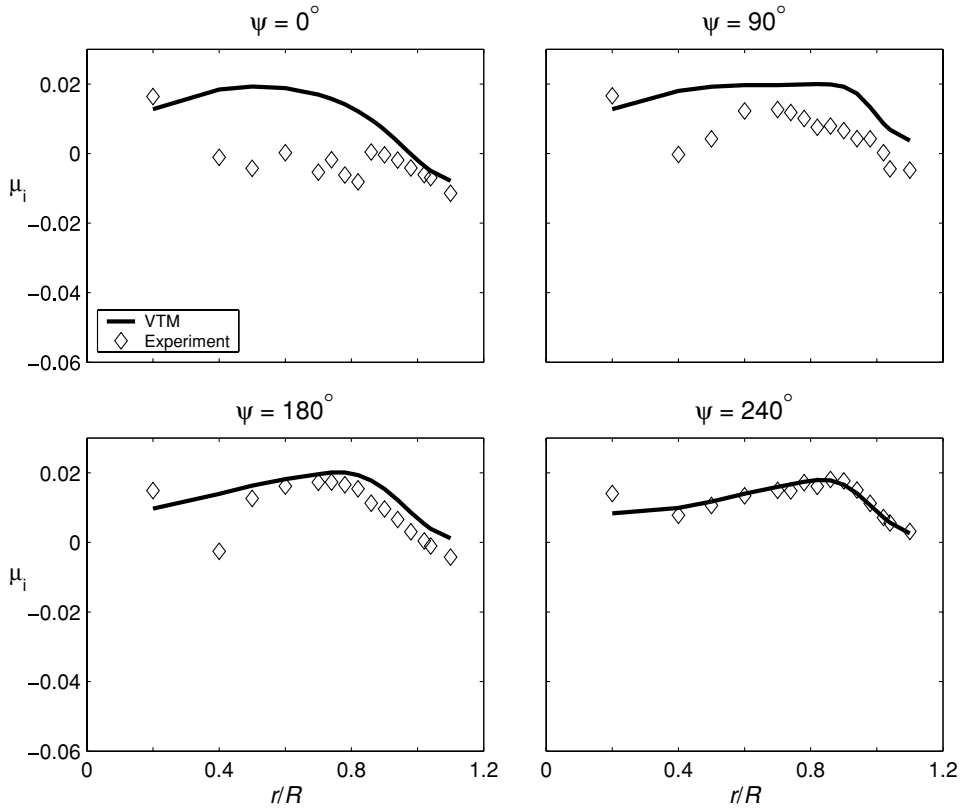

Fig. 13. Mean induced inflow parallel to the TPP ($\mu = 0.15$, $C_T = 0.0064$, measured $1.15c$ above the TPP).

above the TPP, is seen to improve with advance ratio (Figs. 13–15). At low advance ratios, the experimentally measured component of inflow parallel to the TPP reduces abruptly in magnitude around the midspan for locations on the advancing side of the disk, whereas the simulation predicts a smoother trend along the span. At advance ratio $\mu = 0.30$, the correlation between simulation and the induced inflow measured parallel to the TPP is very close, particularly outboard on the rotor. The sudden discontinuity in the radial variation of the experimental results for $\mu = 0.15$ and $\mu = 0.23$ is somewhat unexpected; the time-averaging process used to reduce the experimental results would not be expected to preserve any such abrupt changes in inflow, particularly those that might have plausible physical origin in the geometry of the wake; hence some corruption in the experimental recording process has to be suspected.

At advance ratio $\mu = 0.15$, the normal component of the mean induced inflow $1.15c$ above the TPP predicted by the simulation is in very good agreement with the experimental data over the majority of the rotor disk (Fig. 16). The simulation underpredicts the mean inflow by approximately 50% at midspan at zero degrees of azimuth, however. This location is directly downstream of the rotor hub, and viscous effects such as wake shedding from the hub are again believed to be responsible for some of the discrepancy. The experimental data at azimuthal locations of 60° and 90° show an upwash near the rotor tip that is not well predicted. This observation is consistent with the data presented earlier for the vortex trajectories that suggest an underprediction of the upwash on the advancing side of the rotor disk. The extent of the regions of overpredicted inflow through the rotor disk is reasonably consistent with the region of underpredicted upwash in the analysis of the vortex trajectories. The VTM has been shown before to be intrinsically capable of predicting the initially upward trajectory of the tip vortices of a rotor oriented edge-on to the flow, and thus a small discrepancy between the setup of the simulation and the true experimental conditions is suspected.

The mean induced inflow normal to the TPP at $\mu = 0.23$ compares well with the experimental results with the exception of some areas in the second quadrant of the rotor disk (Fig. 17); compared to the situation at $\mu = 0.15$, the inflow measured $1.15c$ above the TPP in this region of the disk is somewhat overpredicted. This degradation in correlation of the normal component of inflow with advance ratio over the advancing side of the disk was initially considered to be due to underresolution of the rollup of the rotor wake over this part of the rotor. Particularly at high advance ratios, the spanwise gradient of bound circulation is rather shallow, especially around 90° azimuth (see Fig. 18) and consequently the vortex structure that is trailed from the blades in these positions does not consist of a strong tip vortex but rather is a less concentrated structure with a greater spanwise extent. The scales over which this

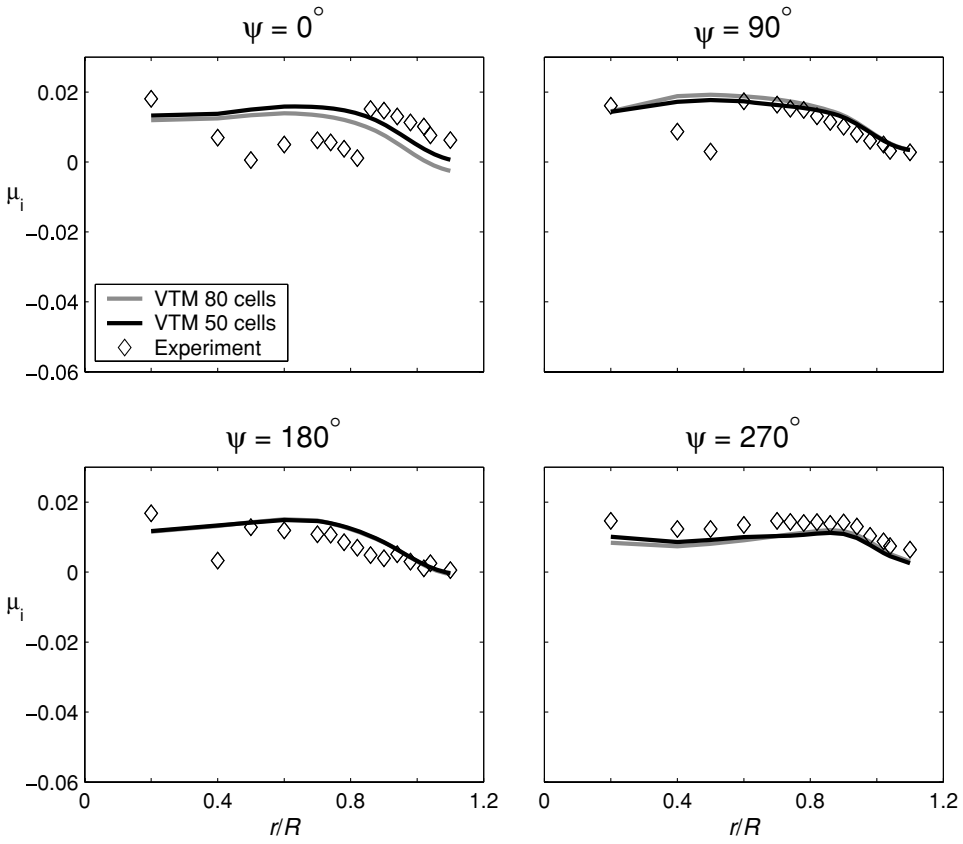

Fig. 14. Mean induced inflow parallel to the TPP ($\mu = 0.23$, $C_T = 0.0064$, measured $1.15c$ above the TPP).

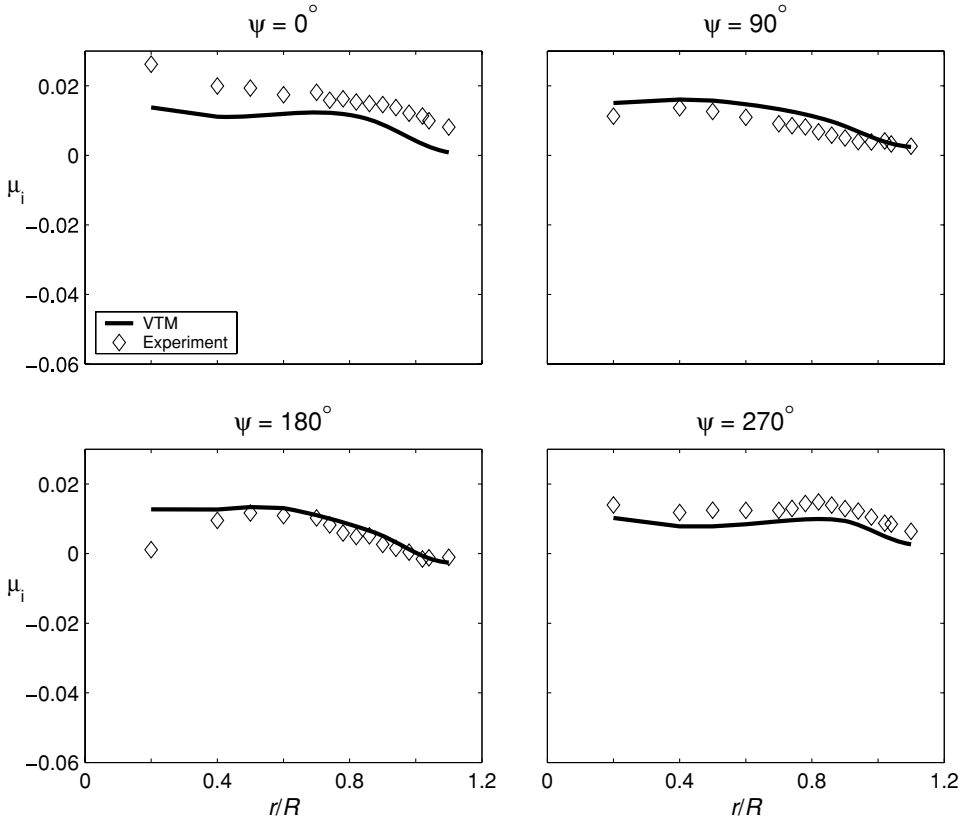

Fig. 15. Mean induced inflow parallel to the TPP ($\mu = 0.30$, $C_T = 0.0064$, measured $1.15c$ above the TPP).

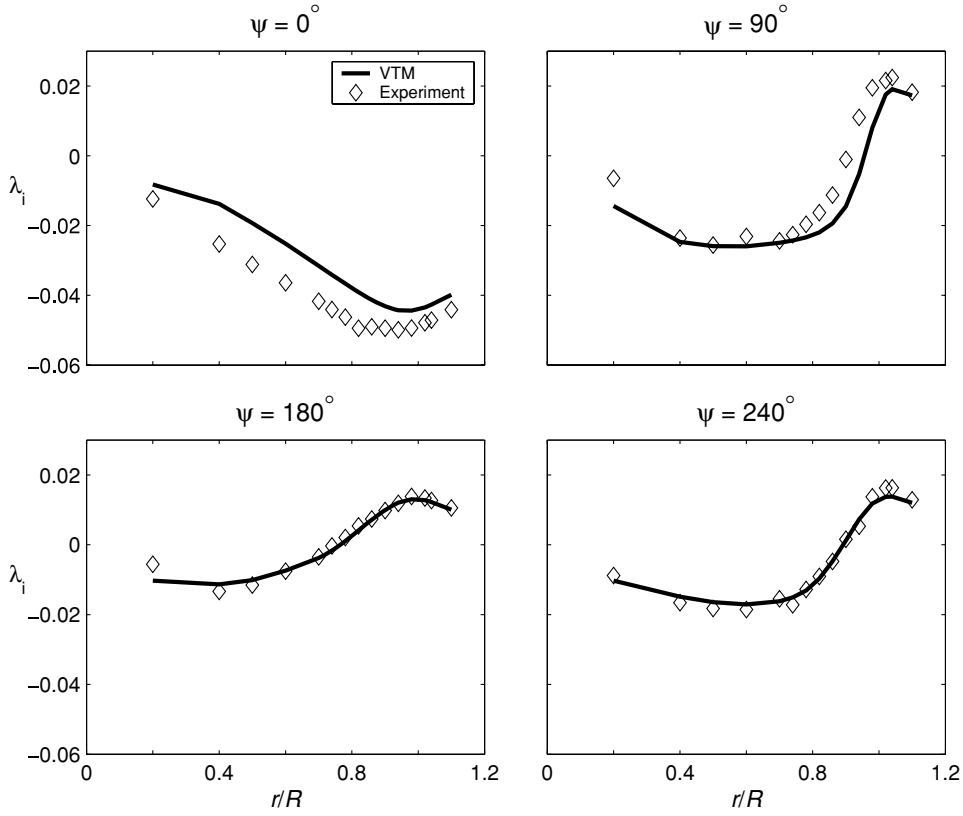

Fig. 16. Mean induced inflow normal to the TPP ($\mu = 0.15$, $C_T = 0.0064$, measured $1.15c$ above the TPP).

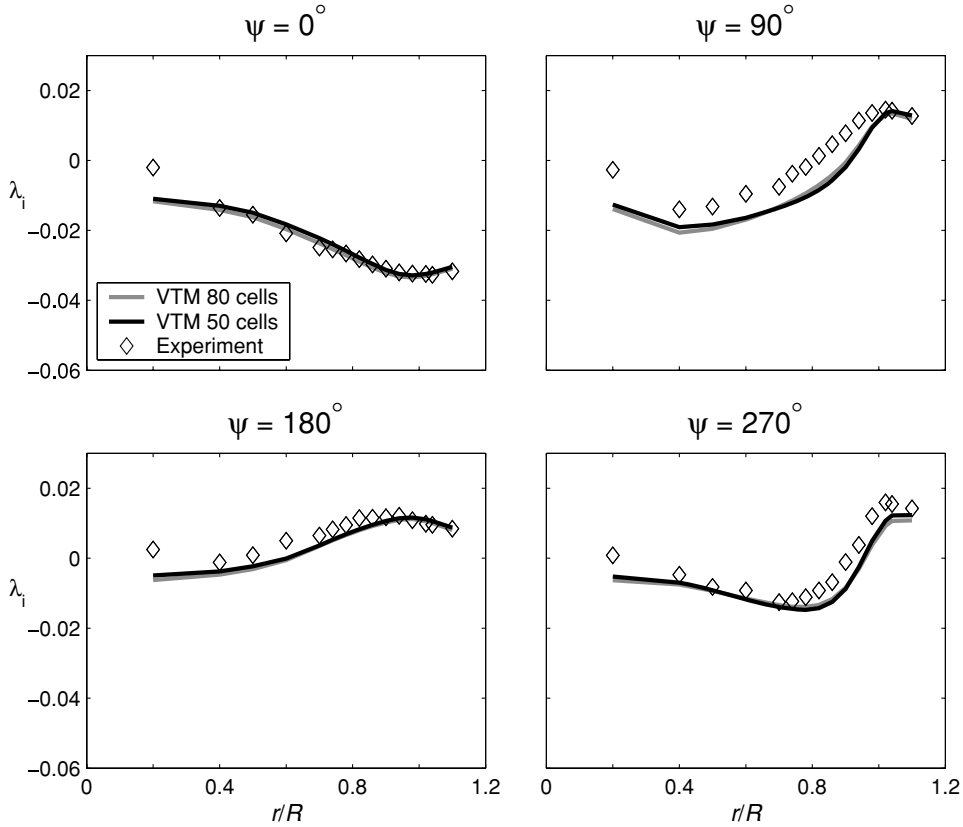

Fig. 17. Mean induced inflow normal to the TPP ($\mu = 0.23$, $C_T = 0.0064$, measured $1.15c$ above the TPP).

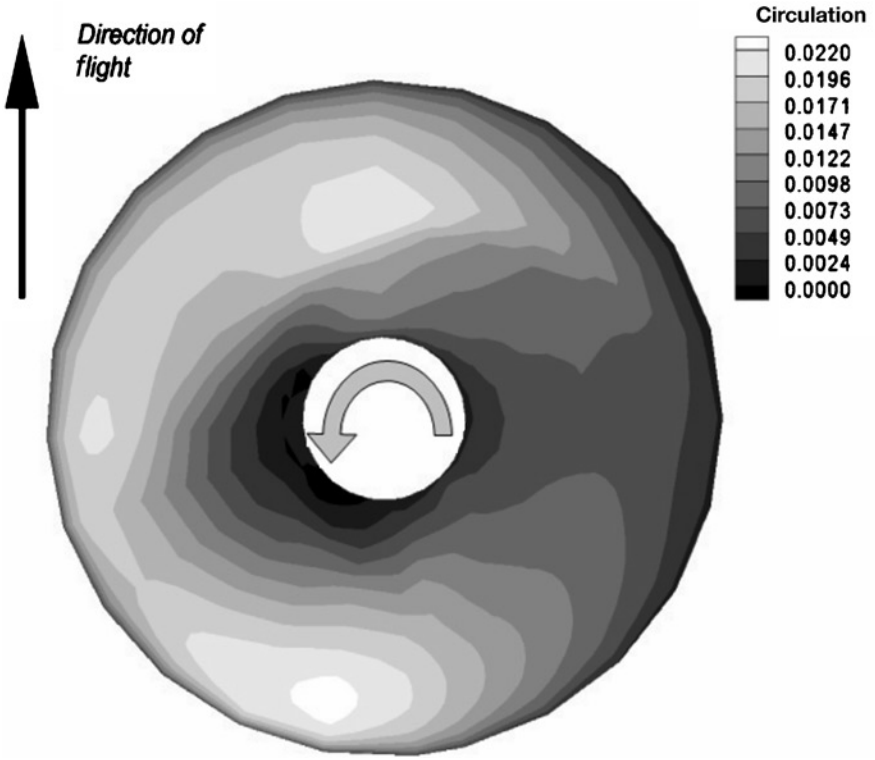

Fig. 18. Variation of nondimensional blade circulation with azimuth ($\mu = 0.30$, $C_T = 0.0065$).

extended vortex structure evolves were believed to be too small for the current grid resolution, i.e., 50 cells per blade radius, to capture. Figures 14 and 17 compare the mean predicted inflow, parallel and normal to the TPP, respectively, for the system operating at advance ratio $\mu = 0.23$, calculated using resolutions of 50 and 80 grid cells per rotor radius. The figures show the increased resolution to yield very little change to the mean induced inflow. This suggests some alternative but as yet unknown source of error in the calculations, but a simple discrepancy in the numerical representation of the experimental setup, as discussed earlier, cannot be ruled out.

At advance ratio $\mu = 0.30$, the inflow normal to the disk in regions close to the hub is consistently overpredicted by the simulation (see Fig. 19). The experimental data show upwash through the disk inboard of $r/R = 0.4$, whereas the VTM predicts downwash through the rotor, at all azimuthal locations. Outboard of these regions of upwash, the simulated data match the experiment well, with the exception again being in the second quadrant where the simulation overpredicts the inflow in a similar fashion to at lower advance ratio.

The possibility cannot be discounted that some or all of the observed discrepancies between the measured and predicted variations in inflow over the rotor disk could simply be due to a small relative error between simulation and experiment in the location of the plane on which the inflow through the rotor was extracted. This error is expected to be small, though, given the very close agreement between the measured and predicted coning angles of the rotor, and the method, described earlier, whereby the plane on which the inflow data were extracted from the simulated flow field was indexed with respect to the TPP of the rotor. The data presented in Fig. 19 allow the effect on the correlation of a possible small error in the location of the measurement plane to be assessed. In this figure, the measured and VTM-predicted inflow at two different heights ($1.15c$ and $0.75c$) above the TPP are presented. At zero azimuth, the simulation is seen to overpredict the inflow measured on the plane $1.15c$ above the TPP, yet at $0.75c$ above the TPP, the magnitude of the simulated data is in good agreement with experiment. In reality, the separation between these two measurement planes is approximately 1 inch, yet the experimentally measured inflow distributions on the advancing side of the rotor change dramatically over this short distance, demonstrating a marked sensitivity of the data to measurement location. The changes in the inflow distributions that are predicted by the VTM over this distance are much more benign. The comparison of inflow on the plane $0.75c$ above the TPP is spoilt in much the same way as at the lower advance ratios, however, by the discontinuities in the experimentally measured inflow around midspan for locations within the second quadrant of the rotor disk. As discussed earlier, these discontinuities in the experimental data are not thought to have physical origin.

The data presented in Figs. 20 and 21 can be compared to shed further insight into the origins of the rather puzzling discrepancy between the quality of the correlation between experiment and the VTM predictions of the inflow on the advancing and retreating sides of the rotor at this forward speed. Figure 20, again comparing the experimental and simulation data at advance ratio $\mu = 0.30$, shows the variation of normal inflow with time, at an azimuth of 300°, on the plane $1.15c$ above the TPP, i.e., at one of the azimuthal locations on the retreating side of the rotor where the predicted mean inflow matches the experimental data reasonably well. The figure shows the unsteady component of the inflow to be predicted to within approximately 5° in phase, and, outboard of $r/R = 0.5$, to within 30% of magnitude, and both the experimental data and the VTM simulations demonstrate clear evidence of the passage of individual blades.

In contrast, Fig. 21 compares the variation of inflow with time at an azimuth of 120°, i.e. at one of the azimuthal locations on the advancing side of the rotor where the VTM predicts significantly greater mean downwash than the experiment. The simulation data are characterized by the presence of clear blade-passage effects at all radial locations inboard of $r/R = 0.90$. Curiously, though, these blade-passage structures are not seen in the experimental data; the measured signal has a more-or-less constant underlying level onto which is superimposed a fair degree

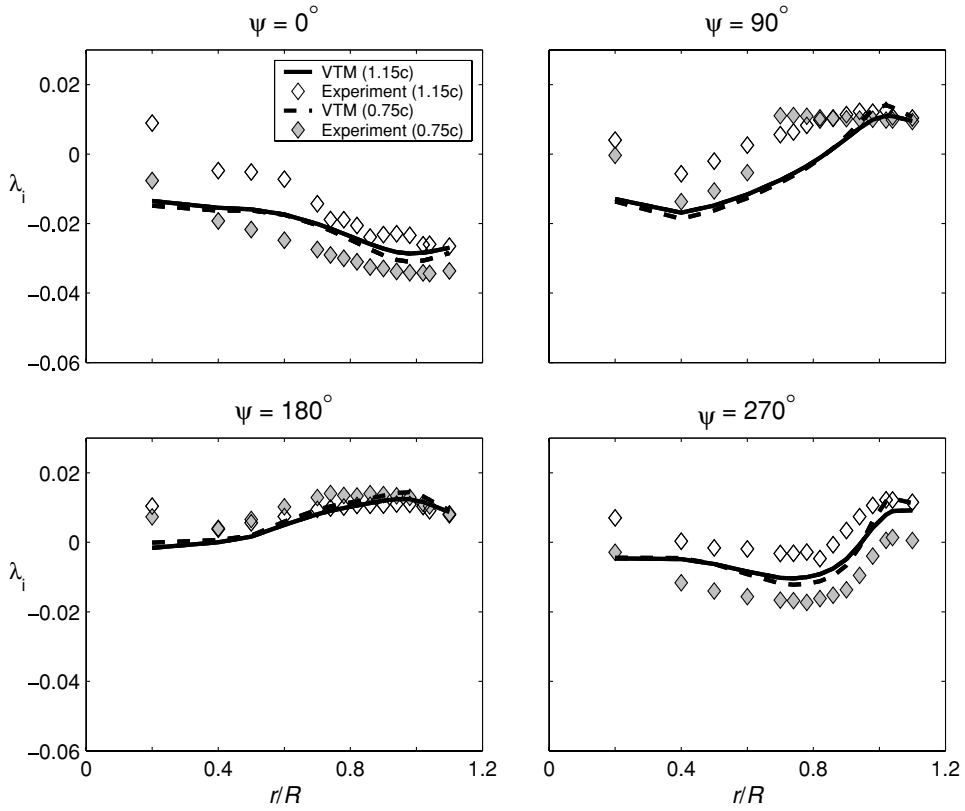

Fig. 19. Mean induced inflow normal to the TPP ($\mu = 0.30$, $C_T = 0.0064$).

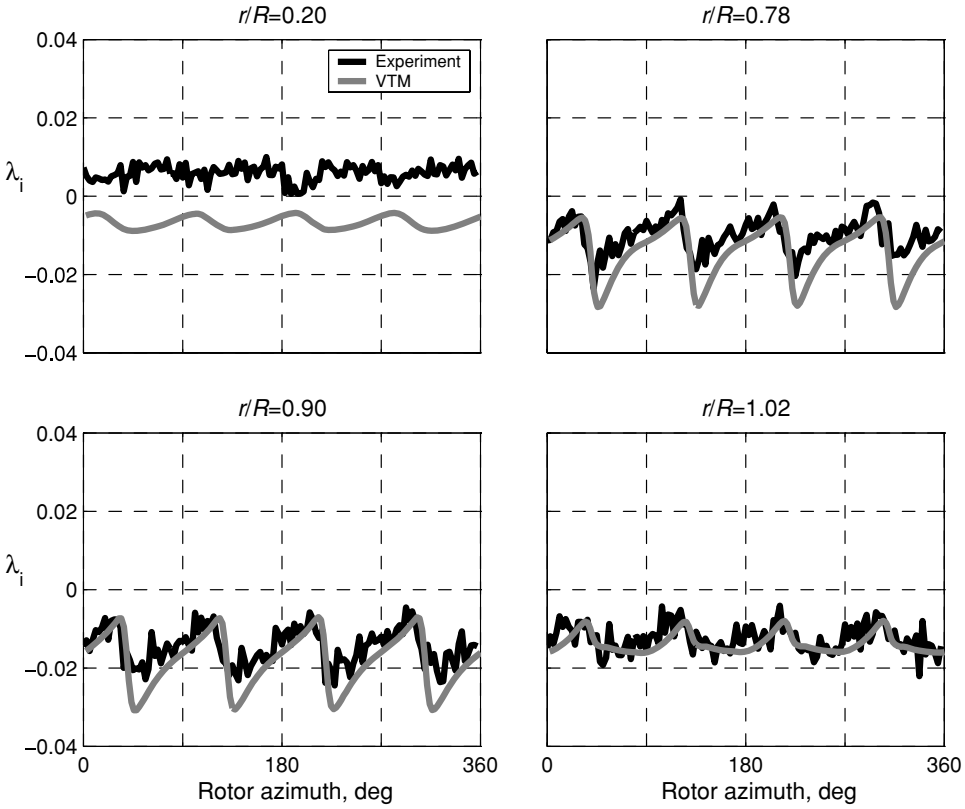

Fig. 20. Variation of induced inflow normal to the TPP with time (rotor azimuth), at a fixed azimuthal location ($\psi = 300°$) where correlation between experimental and predicted mean inflow is good ($\mu = 0.30$, $C_T = 0.0064$, measured $1.15c$ above the TPP).

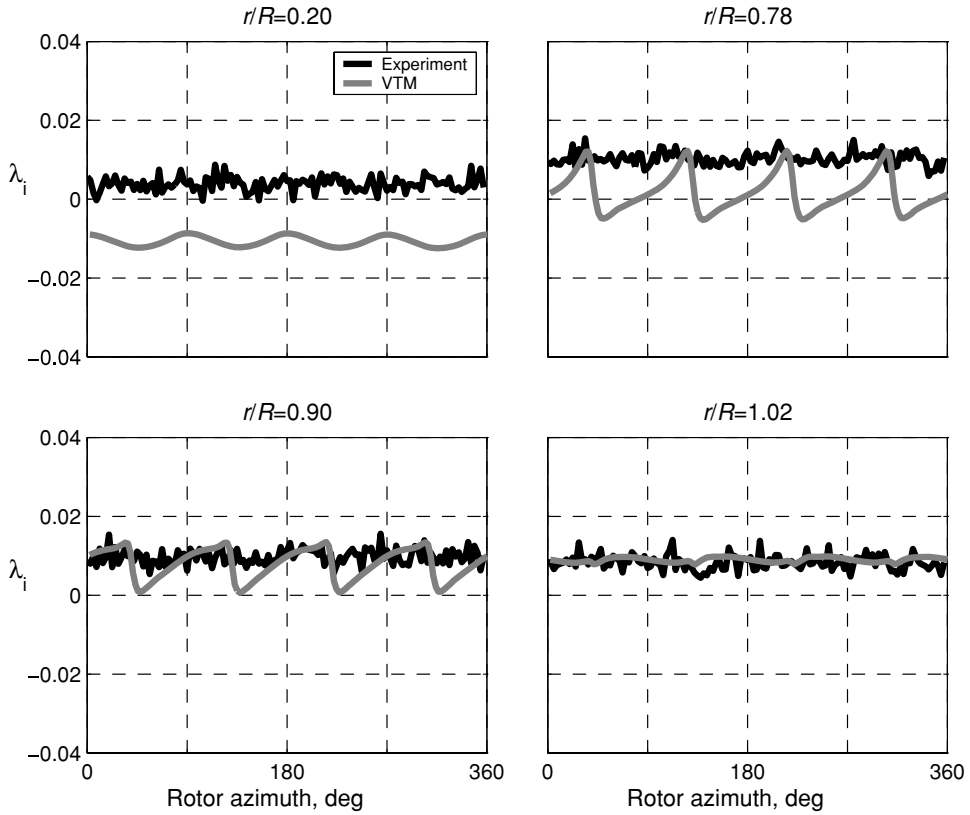

Fig. 21. Variation of induced inflow normal to the TPP with time (rotor azimuth), at a fixed azimuthal location ($\psi = 120°$) where correlation between experimental and predicted mean inflow is poor ($\mu = 0.30$, $C_T = 0.0064$, measured $1.15c$ above the TPP).

of noise. This suggests at face value that this and other, similar, measurement locations in the experiment were not greatly affected by blade passage for some reason, but is also consistent with the presence of flow-seeding problems in the LDV measurements of the inflow. Hence at this stage, it is not possible to state with any certainty what combination of misprediction of vortex trajectories, discrepancy in rotor operating state, and experimental error is responsible for the rather glaring differences between the experimentally measured and numerically predicted inflow normal to the rotor in the second quadrant of the rotor. It is hoped that future comparisons with data measured on other rotor–fuselage geometries will yield further insight.

Conclusion

The aerodynamics of a coupled rotor–fuselage configuration has been studied computationally in an attempt to appreciate the physical processes that govern the aerodynamic interactions within the system. A CFD approach has been employed that uses the vorticity–velocity formulation of the Navier–Stokes equations to evolve, in an unsteady fashion, the wake that is generated by the rotor system. The fuselage was represented using an unsteady panel method. Several of the well-known NASA ROBIN experiments were modeled to investigate the ability of the approach to capture the wake geometry, induced inflow, and fuselage pressure distributions that arise in a tightly coupled rotor–fuselage configuration.

The wake–vortex trajectories predicted by the numerical technique agree well with the experimental smoke-visualization data, especially in terms of the change in wake skew angle with forward flight speed. On the advancing side of the rotor, however, the initial upward trajectory of the tip vortices is somewhat underpredicted.

Nevertheless, the experimentally measured induced inflow both parallel and perpendicular to the TPP is very well predicted by the model at all the advance ratios that were considered in this study. The correlation with experiment of the predicted time-averaged normal inflow does, however, deteriorate somewhat with advance ratio, particularly on the advancing side of the rotor disk. This observation is consistent with the underprediction of the initial upward trajectory of the tip vortices in the same region of the disk, but possible problems with flow seeding in some of the LDV-measured inflow data in this region, and small discrepancies in matching precisely the trim state of the experimental system obscure somewhat the reasons for this discrepancy between experiment and numerics. The numerical technique is capable of predicting very well the experimentally measured variation with time of the inflow through the rotor disk, particularly in those locations where the mean inflow is also well predicted.

The approach is also capable of predicting accurately both the steady and periodic pressure signals on the surface of the ROBIN fuselage; any discrepancies between experiment and simulation are generally found in regions where features of the experiment, such as the fuselage support strut and the rotor hub, have been omitted from the simulation. The ability of the model to track individual vortices as they stream along the surface of the fuselage, and to capture their effect on the distribution of unsteady fuselage pressures, has also been demonstrated.

Acknowledgments

Susan Althoff Gorton and Doug Boyd have assisted this study enormously through the provision of the experimental data and advice on the modeling of their experiments. Their input is greatly appreciated. The

work described in this paper was partly funded through the generous support of QinetiQ plc, Farnborough, UK.

References

[1]Sheridan, P. F., and Smith, R. P., "Interactional Aerodynamics—A New Challenge to Helicopter Technology," *Journal of the American Helicopter Society*, Vol. 25, (1), 1980, pp. 3–21.

[2]Mavris, D. N., Komerath, N. M., and McMahon, H. M., "Prediction of Aerodynamic Rotor–Airframe Interactions in Forward Flight," *Journal of the American Helicopter Society*, Vol. 34, (4), 1989, pp. 37–46.

[3]Lorber, P. F., and Egolf, T. A., "An Unsteady Helicopter Rotor–Fuselage Aerodynamic Interaction Analysis," *Journal of the American Helicopter Society*, Vol. 35, (3), 1990, pp. 32–42.

[4]Bi, N. P., and Leishman, J. G., "Experimental Study of Rotor/Body Aerodynamic Interactions," *Journal of Aircraft*, Vol. 27, (9), 1990, pp. 779–788.

[5]Wachspress, D. A., Quackenbush, T. R., and Boschitsch, A. H., "Rotorcraft Interactional Aerodynamics with Fast Vortex/Fast Panel Methods," *Journal of the American Helicopter Society*, Vol. 48, (4), October 2003, pp. 223–235.

[6]O'Brien, D. M., and Smith, M. J., "Analysis of Rotor–Fuselage Interactions Using Various Rotor Models," AIAA-2005-0468, AIAA 43rd Aerospace Sciences Meeting & Exhibit, Reno, NV, January 10–13, 2005.

[7]Boyd, D. D., and Barnwell, R. W., "A Computational Model for Rotor–Fuselage Interactional Aerodynamics," AIAA-2000-0256, AIAA 38th Aerospace Sciences Meeting & Exhibit, Reno NV, January 10–13, 2000.

[8]Park, Y. M., Nam, H. J., and Kwon, O. J., "Simulation of Unsteady Rotor–Fuselage Interactions Using Unstructured Adaptive Meshes," *Journal of the American Helicopter Society*, Vol. 51, (2), April 2006, pp. 141–149.

[9]Duque, E. P. N., Strawn, R. C., Ahmad, J., and Biswas, R., "An Overset Grid Navier–Stokes/Kirchhoff-Surface Method for Rotorcraft Aeroacoustic Predictions," AIAA-96-0152, AIAA 34th Aerospace Sciences Meeting & Exhibit, Reno, NV, January 15–18. 1996.

[10]Khier, W., Le Chuiton, F., and Schwarz, T., "Navier–Stokes Analysis of the Helicopter Rotor–Fuselage Interference in Forward Flight," presented at the CEAS Aerospace Aerodynamics Research Conference, Cambridge, UK, June 10–12, 2002.

[11]Whitehouse, G. R., Boschitsch, A. H., Quackenbush, T. R., Wachspress, D. A., and Brown, R. E., "Novel Eulerian Vorticity Transport Wake Module for Rotorcraft Flow Analysis," American Helicopter Society 63rd Annual Forum Proceedings, Virginia Beach, VA, May 1–3. 2007.

[12]Mineck, R. E., and Althoff Gorton, S., "Steady and Periodic Pressure Measurements on a Generic Helicopter Fuselage Model in the Presence of a Rotor," NASA TM 2000-210286, June 2000.

[13]Brown, R. E., "Rotor Wake Modelling for Flight Dynamic Simulation of Helicopters," *AIAA Journal*, Vol. 38, (1), 2000, pp. 57–63.

[14]Brown, R. E., and Line, A. J., "Efficient High-Resolution Wake Modelling Using the Vorticity Transport Equation," *AIAA Journal*, Vol. 43, (7), 2005, pp. 1434–1443.

[15]Elliott, J. W., Althoff, S. L., and Sailey, R. H., "Inflow Measurements with a Laser Velocimeter on a Helicopter Model in Forward Flight; Volume I: Rectangular Planform Blades at an Advance Ratio of 0.15," NASA TM 100541, April 1988.

[16]Elliott, J. W., Althoff, S. L., and Sailey, R. H., "Inflow Measurements with a Laser Velocimeter on a Helicopter Model in Forward Flight; Volume II: Rectangular Planform Blades at an Advance Ratio of 0.23," NASA TM 100542, April 1988.

[17]Elliott, J. W., Althoff, S. L., and Sailey, R. H., "Inflow Measurements with a Laser Velocimeter on a Helicopter Model in Forward Flight; Volume III: Rectangular Planform Blades at an Advance Ratio of 0.30," NASA TM 100543, April 1988.

[18]Ghee, T. A., Berry, J. D., Zori, L. A. J., and Elliott, J. W., "Wake Geometry Measurements and Analytical Calculations on a Small-Scale Rotor Model," NASA TP 3584, August 1996.

[19]Freeman, C. E., and Mineck, R. E., "Fuselage Surface Pressure Measurements of a Helicopter Wind-Tunnel Model With a 3.15-Meter Diameter Single Rotor," NASA TM 80051, March 1979.

[20]Phelps, A. E., III, and Berry, J. D., "Description of the U. S. Army Small-Scale 2-Meter Rotor Test System," NASA TM 87762, February 1987.

[21]Althoff Gorton, S., and Hoad, D. R., "Assessment of Rotor Blade Angle of Attack from Experimental Inflow Data," *Journal of Aircraft*, Vol. 39, (5), September–October 2002, pp. 722–730.

[22]Boyd, D. D., Personal communication, August 15, 2006.

[23]Mineck, R. E., "Application of an Unstructured Grid Navier–Stokes Solver to a Generic Helicopter Body," NASA TM 1999-209510, August 1999.

[24]Liou, S. G., Komerath, N. M., and McMahon, H. M., "Measurement of the Interaction Between a Rotor Tip Vortex and a Cylinder," *AIAA Journal*, Vol. 28, (6), June 1990, pp. 975–981.

[25]Althoff, S. L., Elliott, J. W., Hoad, D. R., and Sailey, R. H., "Inflow Measurements with a Laser Velocimeter on a Helicopter Model in Forward Flight; Volume IX: Rectangular Planform Blades at an Advance Ratio of 0.23, 0.75 Chord Above the Tip Path Plane," NASA TM 102643, May 1990.

[26]Althoff, S. L., Elliott, J. W., Hoad, D. R., and Sailey, R. H., "Inflow Measurements with a Laser Velocimeter on a Helicopter Model in Forward Flight; Volume XI: Rectangular Planform Blades at an Advance Ratio of 0.30, 0.75 Chord Above the Tip Path Plane," NASA TM 102645, May 1990.